




Article

Novel Multicomponent B2-Ordered Aluminides: Compositional Design, Synthesis, Characterization, and Thermal Stability

G. Mohan Muralikrishna ^{1,2,*} , A. Carmel Mary Esther ² , K. Guruvidyathri ³ , Philipp Watermeyer ⁴, Christian H. Liebscher ⁴, Kaustubh N. Kulkarni ⁵, Gerhard Wilde ², Sergiy V. Divinski ^{2,*} and B. S. Murty ^{1,6,*}

¹ Department of Metallurgical and Materials Engineering, Indian Institute of Technology Madras, Chennai 600036, India

² Institute of Materials Physics, University of Muenster, 48149 Muenster, Germany; carmelnano@gmail.com (A.C.M.E.); gwilde@wwu.de (G.W.)

³ School of Engineering Sciences and Technology, University of Hyderabad, Gachibowli, Hyderabad 502285, India; guruvidyathri@gmail.com

⁴ Max Planck Institute für Eisenforschung GmbH, Max-Planck-Straße 1, 40237 Düsseldorf, Germany; p.watermeyer@mpie.de (P.W.); liebscher@mpie.de (C.H.L.)

⁵ Department of Materials Science and Engineering, Indian Institute of Technology Kanpur, Uttar Pradesh 208016, India; kkaustub@iitk.ac.in

⁶ Indian Institute of Technology Hyderabad, Kandi 502285, India

* Correspondence: mohanmuralikrishna9@gmail.com (G.M.M.); divin@uni-muenster.de (S.V.D.); murty@iitm.ac.in (B.S.M.); Tel.: +91-8374-338-979 (G.M.M.); +49-251-8339030 (S.V.D.); +91-040-2301-6001 (B.S.M.)

Received: 1 October 2020; Accepted: 20 October 2020; Published: 23 October 2020



Abstract: For the first time, multicomponent alloys belonging to a B2-ordered single phase were designed and fabricated by melting route. The design concept of high entropy alloys is applied to engineering the transition metal sublattice of binary B2 aluminide. The equiatomic substitution of transition metal elements in the Ni sublattice of binary AlNi followed to produce Al(CoNi), Al(FeNi), Al(CoFe), Al(CoFeNi), Al(CoFeMnNi), and Al(CoCuFeMnNi) multicomponent alloys. CALPHAD approach was used to predict the phases in these alloys. X-ray diffraction and transmission electron microscopy were used to confirm the B2 ordering in the alloys. Thermal stability of the B2 phase in these alloys was demonstrated by prolonged heat treatments at 1373 K and 1073 K up to 200 h.

Keywords: multicomponent alloys; high entropy alloys; intermetallic compound; B2; aluminide; CALPHAD; phase diagrams; HRTEM; thermal stability

1. Introduction

High entropy alloys (HEAs) represent a new class of materials containing multiple principal elements in (generally) near-equiatomic compositions. HEAs were reported to have fascinating properties such as superior strength–ductility trade-off [1,2], high thermal stability [3], corrosion resistance [4], wear resistance [5], enhanced resistance to oxidation [6], good hot deformation behavior [7], etc. The proposed four core effects were hypothesized in [8] to be responsible for these superior properties, and they are being studied extensively.

HEAs were initially expected to form single-phase solid solutions due to the high configurational entropy caused by the presence of multiple elements [9]. However, numerous investigations have

shown the presence of multiple phases [10,11]. The existence of a single-phase solid solution at room temperature was observed for the CoCrFeMnNi HEA system, also known as the Cantor alloy [12]. However, this alloy showed the precipitation of second phases, e.g., the sigma phase after heat treatment at non-ambient temperatures [13–15]. Several HEAs containing Al form B2/L1₂ ordered intermetallic compounds as secondary phases or precipitates [16–18].

Recent reports showed that the presence of B2 phases could improve the overall mechanical properties of the alloys [19–22]. Al_{0.5}CoCrCuFeNi was reported to have almost equal phase fractions of FCC and BCC/B2 phases, exhibiting high yield strength [23]. The AlCoCrFeNi HEA containing B2 precipitates was found to have improved oxidation resistance [24].

The tribological properties of the AlCoCrFeNiTi_{0.5} HEA were reported to be better than Fe₇₇Ni₂₃ and TiAl₄₆Cr₂Nb₂ intermetallic compounds. This is mainly attributed to the presence of the Al-Ni-Ti intermetallic phases [5]. The increased fraction of the B2 phase with an increase in Al concentration was observed for the AlCoCrCuFeNi system and was found to enhance the mechanical properties. A very high specific hardness of 160 HVg⁻¹cm⁻³ was reported for Al-containing HEAs and was attributed to the increased atomic ordering along with the solid solution strengthening that are enhancing the superior mechanical properties over INCONEL 718 [3]. Thus, the freedom to vary elemental compositions facilitates fine tuning the mechanical properties. Most of the aforementioned studies mainly focused on HEA compositions forming multiple phases, but the reports on single-phase HEAs are lacking in the literature.

Furthermore, B2 aluminides are well known for their high strength, resistance to high-temperature oxidation, and high melting points [25]. Due to the stability of the B2 structure coupled to very high melting temperatures, B2 aluminides are known to retain their properties up to high temperatures [26,27]. The atomic order in intermetallic compounds such as AlNi, AlCo, and AlFe is known to slow down diffusion by retaining a long-range order at high temperatures [28,29]. Major applications of the B2 aluminides include combustor liners, air deflectors in burners, turbine vanes, and heat transfer rolls. However, their usage was limited due to their lower ductility and fracture toughness at room temperatures [25]. The B2-ordered phases are generally hard and brittle. However, their utilization as secondary phase inclusions has been frequently shown to represent a suitable approach to improve the mechanical and functional properties of complex alloys. Although the presence of a B2 phase was reported in several multicomponent alloys/HEAs [3–10], there are no reports on the design of the multicomponent alloys consisting of a single-phase B2 structure. The high-entropy concept allows us to explore new possibilities in alloy design to retain acceptable ductility. Hence, the design of novel, multicomponent, single-phase B2-ordered alloys will advance our understanding on the impact of compositional complexity on ordered phases and their application as potential high temperature materials.

With this motivation, the present study focuses on the design, synthesis, characterization, and phase stability of multicomponent B2 aluminides. In order to systematically understand the crystallographic lattice/order parameter changes of multicomponent systems as a function of the number of elements, the formation of single-phase binary to ternary alloy systems is necessary. Therefore, from the obtained knowledge through literature and owing to the anticipated good mechanical behavior, a possible single-phase B2 solid solution formation from binary to ternary alloys is derived and aimed for in the current study. Selected properties, especially volume diffusion, have been published already for some of the alloys [29,30], and the achieved exciting properties motivated us for a conceptual development of a systematic alloy design.

The compositional design involves matching element identification and CALPHAD studies. Additionally, the equi-substitution on a selected sublattice to achieve entropy maximization (pseudo-binary approach) is also adopted, which was demonstrated in [31] to be successful for metallic glasses. The present alloy design holds another technological importance of reduced overall alloy density by increasing the number of elements in equiatomic proportion by substituting the Ni sublattice alone. Hence, the motivation for the current study is to achieve lightweight and higher entropically configured multicomponent alloys along with a systematic characterization.

2. Compositional Design

Phase diagrams are the roadmaps for compositional design. Since in HEA composition region the phase diagrams are scarce, several empirical rules are in use [32]. These methods are simple and useful but have significant inaccuracies. Binary phase diagrams are available, which can be inspected to draw some useful insights. Zhang et al. have proposed a two-step method involving phase diagram inspection as the first step [33]. In this, matching elements are identified and are expected to form a targeted single phase in HEA regime. The second step is to use the CALPHAD method for phase diagram calculation, developing Gibbs energy databases if necessary. These two steps are adopted in the present study. Additionally, the entropy maximization of the transition metal (TM) sublattice using equiatomic substitution is an essential aspect of the present composition design for increased stability of the B2 phase.

2.1. Matching Elements Identification

The targeted single phase is B2 in the present work. Reasonably large B2 phase regions exist in binary systems Al-Ni, Al-Co, and Al-Ni at near equiatomic compositions [34]. Thus, the role of Al is profound in B2 phase formation. Mn was found to form B2 in a Mn-Ni system and Cu in a Cu-Zn system, although occupying only a smaller range in the phase diagram [35]. The identified matching elements are thus, Al, Ni, Co, and Fe along with Mn and Cu.

2.2. Pseudo-Binary Approach for Entropy Maximization

The formation of B2 phases is well understood in binary alloys near stoichiometric compositions. Therefore, by combining these binary systems, three ternary systems that have a potential to form B2 compounds can be obtained. Combining them with equal molar fractions will naturally yield a nonequiatom ternary alloy with 50 at.% Al and the other two elements together featuring 50 at.%. Therefore, Al(CoNi), Al(FeNi), and Al(CoFe) are the ternary alloys. In the same way, a quaternary Al(CoFeNi) can also be designed. The individual amount of transition metals (TM) decreases from 25 at.% in ternary to 16.67 at.% in quaternary.

In a quinary, the TM content will further decrease to 12.5 at.%. Accordingly, as the fifth element, Mn was selected. It is possible that it dissolves in the B2 phase, occupying TM sublattice sites, resulting in the Al(CoFeMnNi) compound. Although Cu-Al forms a complex η -phase at equiatomic composition, a B2 phase exists in the Cu-Zn system [30]. In view of these reasonings, Cu was selected as a sixth elemental addition. A 10 at.% of Cu might be expected to result in Al(CoCuFeMnNi). Thus, the selected alloys based on a heuristic matching element approach are Al(CoNi), Al(CoFe), Al(FeNi), Al(CoFeNi), Al(CoFeMnNi), and Al(CoCuFeMnNi). It is worth noting that the formula resembles a two-sublattice system similar to, for example, AlNi. Hence, these alloys can be called pseudo-binary alloys or pseudo-binary B2 aluminides. In this design stage, it is hypothesized that the B2 phase will have similar two sublattices experimentally. Since an understanding of binary B2 phase is well established, Al(Ni) was selected in the present study as the only binary for assessing the experimental conditions against other studies.

2.3. Phase Diagrams from CALPHAD

Whether the chosen alloys will result in a single-phase B2 structure or not can be more rigorously predicted by CALPHAD studies. An added advantage in these alloys is that the TM sublattice has equiatomic substitution. This will maximize the configurational entropy calculated for this sublattice using the sublattice formalism of CALPHAD method [36]. However, in case the enthalpy and nonideal entropy contributions dominate, the B2 phase may not even appear as a stable phase.

A systematic CALPHAD investigation of alloys was carried out. Al concentration was maintained at 50 at.%, since the role of Al is profound in B2 phase formation. The rest of the composition that is composed of Co, Cu, Fe, Mn, and Ni or any other elemental addition is made in the rest of the 50 at.%

This is based on the hypothesis that Al occupies one sublattice and the transition metal elements occupy another sublattice. The isopleth sections were calculated to find the homogeneity range in the ternary and quaternary space for the B2 phase using the Thermo-Calc software (Thermo-Calc, Solna, Sweden) with the TCHEA2 database. The TCHEA2 database was developed using the framework of 20 elements considering all stable phases after assessing the systems, including the present elements. In this database, the thermodynamic stability for the phases A2, B2, A1, and L1₂ were modelled with a two-sublattice model and critically assessed with the experimental results. The formation of intermetallic phases and their solid solubilities were also assessed [37,38].

First-principles approaches such as density functional theory calculations are widely applied in alloy design [11,39–41]. However, they are not yet a part of routine phase diagram calculations due to the enormous computational effort, especially with respect to fully addressing finite temperature effects in concentrated multicomponent alloys containing multiple phases with complex crystal structures.

Figure 1a–c presents the calculated isopleths of Al₅₀Ni_xCo_{50-x}, Al₅₀Ni_xFe_{50-x}, and Al₅₀Co_xFe_{50-x}, named as Al(Co,Ni), Al(Fe,Ni), and Al(Co,Fe). For example, Al(Co,Ni) indicates that the concentration of Al is maintained at 50 at.% atomic fraction, while Co and Ni are varied between 0 to 50 at.%. Similarly, isopleth sections were calculated for the quaternary Al(Co,Fe,Ni) system. The calculated isopleth sections with varying composition of two-constituent elements Al(Ni-Co,Fe), Al(Co-Fe,Ni), and Al(Fe-Co,Ni) are presented in Figure 2a–c. For example, in Al(Ni-Co,Fe), Al and Fe were kept at 50 and 16.67 at.%, respectively, while Ni and Co vary from 0 to 33.33 at.%. In these ternary and quaternaries, a wide range of composition space for B2 phase was observed. A stable B2 phase was observed over large temperature ranges from 700 K until the melting point for the entire composition range of the chosen ternary and quaternary systems.

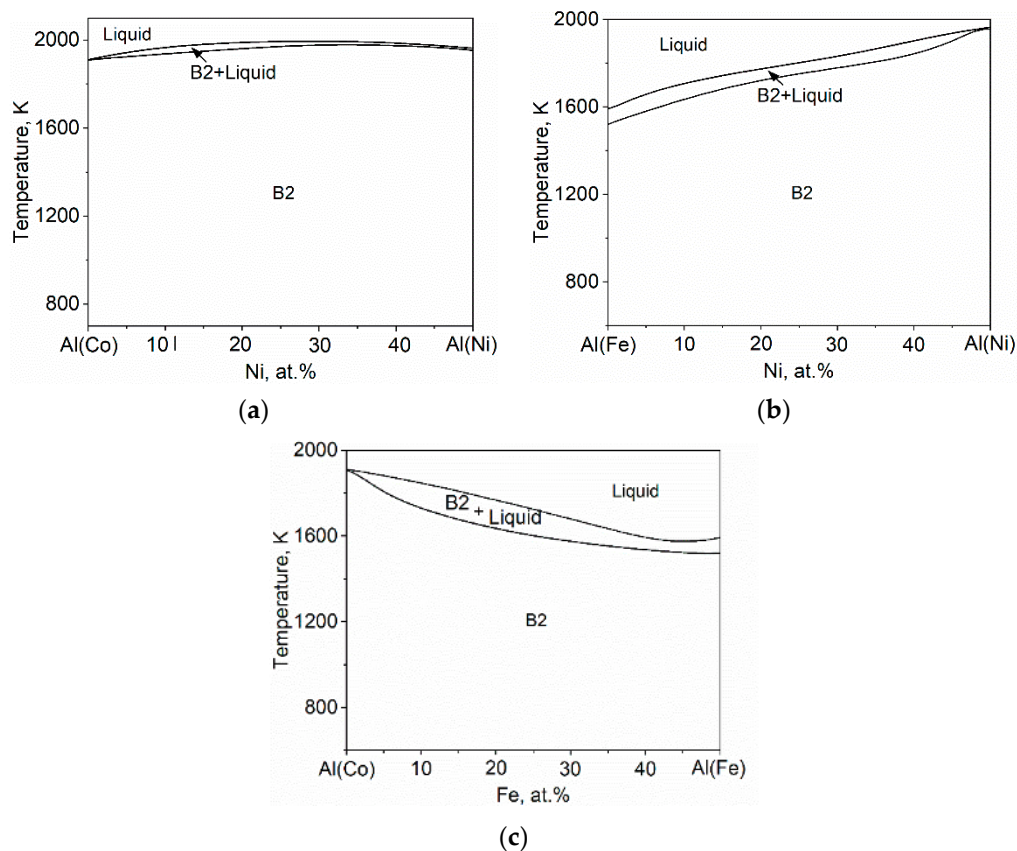


Figure 1. Calculated isopleth sections of (a) Al(Co,Ni), (b) Al(Fe,Ni), and (c) Al(Co,Fe) ternary alloys.

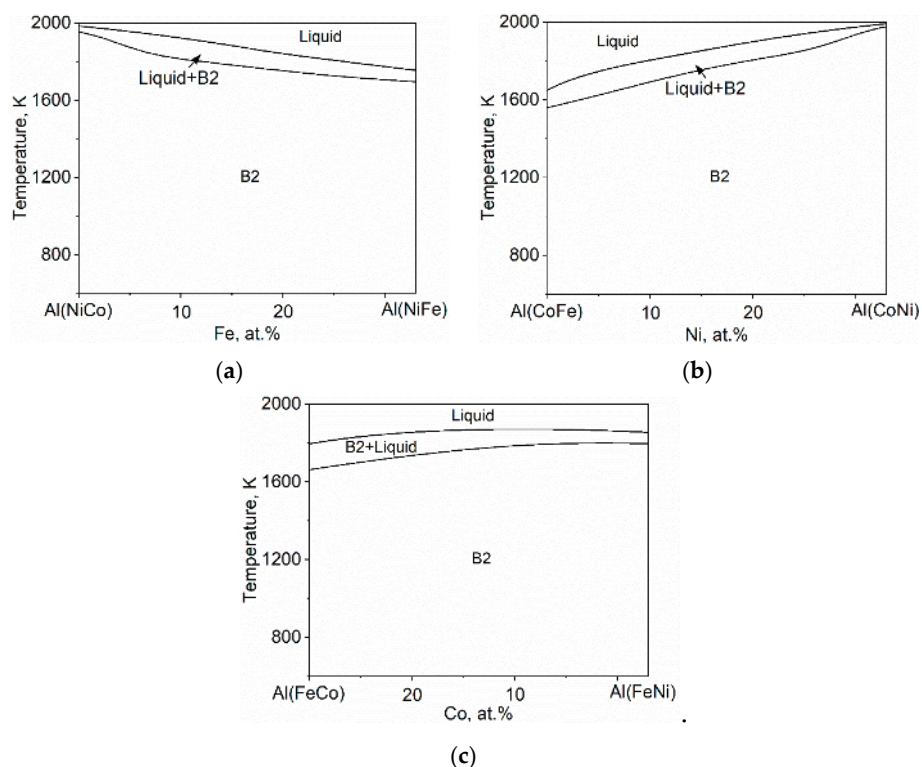


Figure 2. Calculated isopleth sections in the Al(Co,Fe,Ni) system as a function of (a) Fe; (b) Ni; (c) Co.

In principle, any composition in these domains is capable of producing a single-phase B2, including the pseudo-binary compositions, due to the possible entropy maximization effect. Hence, the pseudo-binary alloy compositions viz. ternary Al(CoNi), Al(CoFe), Al(FeNi), and quaternary Al(CoFeNi) were selected with more confidence for further experiments. Mn was calculated to dissolve in a single-phase B2 compound when added as the fifth element in the TM sublattice.

Again, equi-substitution was used for possible entropy maximization vis-à-vis the dissolution of Mn in B2 phase formaton in this alloy. For this reason, a multicomponent alloy in quinary space, Al(CoFeMnNi), was selected for further experiments. Similarly, Cu dissolved in a B2 phase for a sufficiently wide temperature range, and thus Al(CoCuFeMnNi) was selected as a senary alloy. Figure 3a,b shows the phase fraction plots for quinary and senary alloys, showing the presence of a single-phase B2 compound.

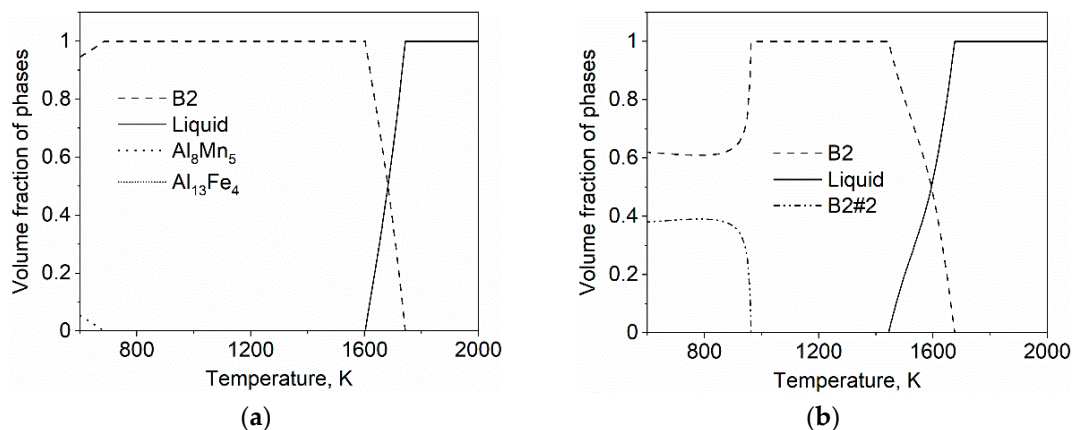


Figure 3. Calculated phase fraction plot for (a) quinary Al(CoFeMnNi); (b) senary Al(CoCuFeMnNi).

3. Materials and Methods

High purity (>99.5%) elemental pieces/flakes/granules of Al, Co, Cu, Fe, Mn, Ni were used in required proportions to prepare the AlNi, Al(CoNi), Al(CoFe), Al(FeNi), Al(CoFeNi), Al(CoFeMnNi), and Al(CoCuFeMnNi) multicomponent B2 aluminides. The concentration of Al in the alloys was maintained at 50 at.%, and the remaining elements in the transition metal sublattice were taken in equiatomic proportions. The proposed alloys were prepared using vacuum arc melting. The melting chamber was evacuated (10^{-5} mbar) and filled with high purity (99.99%) Ar gas. A pure titanium getter was heated before the melting of the alloys to trap the tracers of oxygen inside the chamber if any. The samples were re-melted at least 5 times to achieve a homogenous distribution of the elements. The samples were flipped upside down before each re-melting. The arc-melted buttons were suction casted into 8 mm diameter rods using a copper mould.

The as-cast alloys were subjected to a homogenisation treatment. The heat treatments were performed carefully under a high purity Ar atmosphere to minimize the elemental losses or secondary reactions such as oxidation or reaction of samples with quartz (SiO_2). To prevent these secondary reactions, the suction-casted rods were wrapped in thin (0.025 mm) Ta foil of purity 99.9% and sealed inside an evacuated (5×10^{-5} mbar) and Ar filled (220 mbar) quartz tube. The sealed quartz tubes were subjected to homogenisation heat treatment at 1373 K for 144 h (6 days). Annealing at a high temperature and for a long time was essential to obtain dendrite-free homogenous microstructures. Homogenised samples were cut into 1 mm thick samples using contact free wire erosion cutting machine (AG für industrielle Elektronik (AGIE), Losone-Locarno, Switzerland) with a current of 120 mA; nonflammable organic oil was used as a coolant. The obtained samples were polished to a mirror-like finish using standard metallographic techniques.

Identification of phases was performed using X-ray diffraction (XRD, PANalytical XPert PRO B.V., Almelo, The Netherlands) on powder samples using Cu $K\alpha$ radiation ($\lambda = 0.154$ nm), with an accelerating voltage of 40 kV and a current of 40 mA. The bulk samples were ground to fine powder in a hand grinder and used for X-ray diffraction. Diffractograms were acquired at a step size of 0.02° , a count time of 20 s per step using a diffractometer with Bragg–Brentano geometry, and an area detection diffracton system. The thermal analysis was carried out to determine the melting point by a differential thermal analysis (DTA, SETARAM TGA-DSC 1600, SETARAM Labsys evo, France). The microstructure of the alloys and the chemical composition were examined using scanning electron microscopy (SEM, FEI Nova NanoSEM 230, The Netherlands) attached with energy dispersive spectroscopy (EDS). The elemental concentrations were determined using ZAF quantification route. Samples for scanning transmission electron microscopy (STEM) were extracted from the material by focused ion beam preparation in a dual-beam Scios 2 HiVac (Thermo Fisher Scientific, Waltham, MA, USA) instrument. To protect the area of the sample region to be investigated, a protective layer of platinum (Pt) was deposited by electron and ion beam deposition. Trenches were milled on both sides of the Pt layer with decreasing currents from 50 nA to 1 nA, leaving a lamella with dimensions of $20 \times 1.5 \times 10 \mu\text{m}^3$. The lamella was transferred by in situ liftout (Easy-Lift) and welded to a copper (Cu) grid. The sample was thinned to electron transparency on both sides at 30 kV Ga-ion energy with decreasing beam currents from 1 nA to finally 100 pA. In the final step, the lamella was polished with a beam current of 48 pA and 5 kV Ga-ion energy. High resolution scanning transmission electron microscopy (STEM) and corresponding EDS measurements were performed on the quinary and senary B2 aluminides using an aberration-corrected transmission electron microscope Titan Themis 60-300 (Thermo Fisher Scientific, Waltham, MA, USA) operated at an acceleration voltage of 300 kV. A probe semiconvergence angle of 23.8 mrad was used at a probe current of ≈ 70 pA. The inner and outer collection angles of the high angle annular dark-field (HAADF) detector were set to 73 and 200 mrad respectively for HAADF-STEM imaging. An individual image is the average of an image series of 100 images acquired at a pixel dwell time of $0.5 \mu\text{s}$. The images in the series were aligned by rigid registration and averaged to reduce the influence of fast scan noise. A 4-quadrant EDS system (ChemiSTEM system, Thermo Fisher Scientific,

Waltham, MA, USA) was employed for STEM-EDS measurements with a total solid angle of 0.7 sr, and the probe current was raised to 233 pA and 281 pA for the quinary and senary alloys, respectively.

4. Results and Discussion

4.1. Characterization of Multicomponent B2 Aluminides

The microstructures of the as-cast samples reveal a heterogeneous structure with dendritic and interdendritic regions. An example of typical microstructure and the concentration maps obtained by EDS are presented for the as-cast Al(CoFeMnNi) quinary alloy in Figure 4. Segregation of Mn along the interdendritic regions is seen from Figure 4. It is typical that the solidified alloys contain inhomogeneities due to fast/nonequilibrium cooling. Hence, a homogenisation treatment is inevitable.

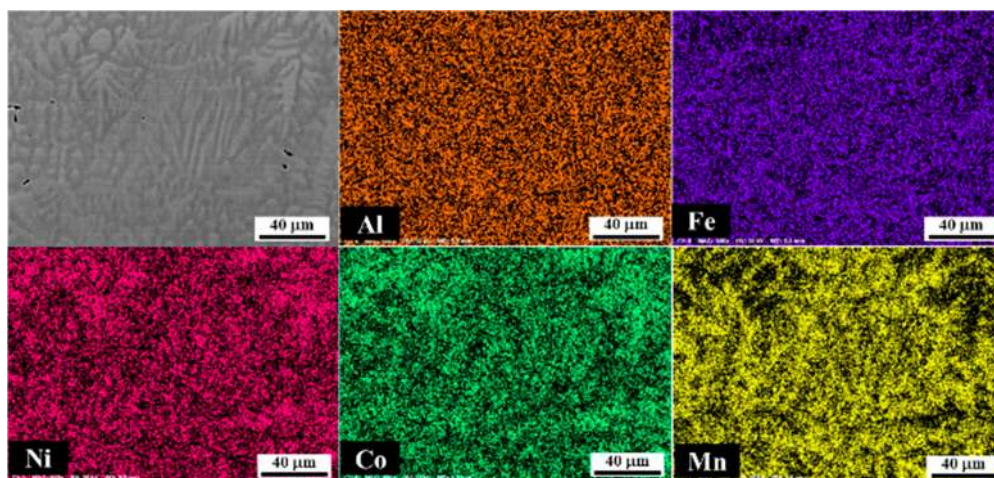


Figure 4. Typical microstructure and elemental mapping of the as-cast Al(CoFeMnNi) quinary alloy exhibiting dendritic microstructure.

4.1.1. Structural Characterization Using X-ray Diffraction Techniques

The structural characterisation of the homogenised samples was carried out using X-ray diffraction. The XRD patterns of the synthesised aluminides ranging from binary to senary are presented in Figure 5a,b. The X-ray diffraction patterns (Figure 5b) of the processed samples substantiated the presence of monolithic ordered B2 phase, and no second phases were found.

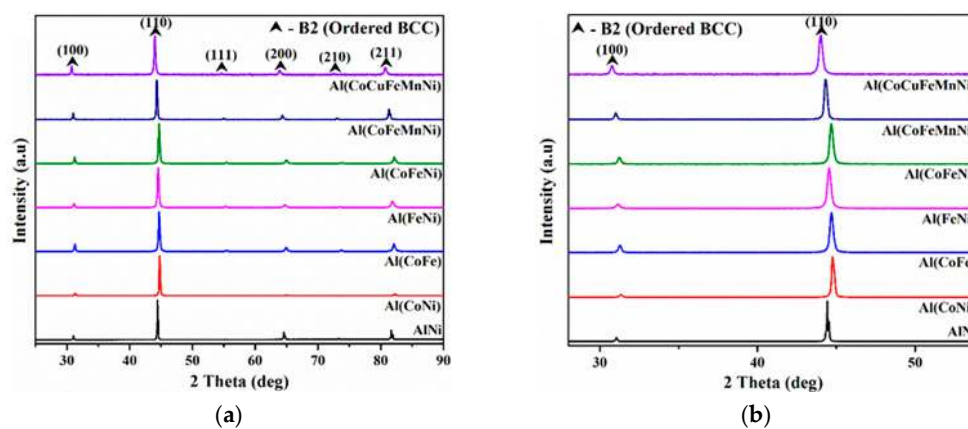


Figure 5. (a) X-ray diffractograms of pseudo-binary multicomponent alloys homogenized at 1373 K for 144 h showing the ordered BCC (B2) structure. (b) Slow scanned X-ray diffractograms showing a superlattice reflection (100).

The XRD patterns confirm the presence of a B2 phase as predicted by the CALPHAD method. The appearance of superlattice reflections of (100), (111), and (210) substantiates the presence of B2 chemical ordering in the alloys. It is well known that all the crystallographic planes of B2 phase can contribute to the diffraction [42]. Thus, superlattice reflections will be visible along with the fundamental diffraction peaks similar to BCC. X-ray reflections of (100), (111), and (210) planes are forbidden in a typical BCC phase due to the crystallographic symmetry [42]. Hence, there is a good correlation of experimental and theoretical calculations of the alloys in the present study.

The long-range order parameter can be estimated using the intensity (I) ratio of the superlattice to fundamental diffraction peaks [42] using the equation below:

$$L = \frac{\sqrt{\left(\frac{I_{100}}{I_{110}}\right)_{sample}}}{\sqrt{\left(\frac{I_{100}}{I_{110}}\right)_{standard}}} \quad (1)$$

The standard database is not available for these novel multicomponent alloys/aluminides. Owing to the long-range order parameter relationship $L \propto I_{100}/I_{110}$, the ratios of the integrated intensities can be an effective parameter to understand the extent of the order in the lattice. Table 1 shows the estimated order parameters of the present alloys. The order parameter was estimated for the binary and ternary alloys where the standard database is available. The long-range order parameter (L) with the relative intensity ratios (I_{100}/I_{110}) are best fitted ($R^2 = 0.99$) in a linear function as shown below:

$$L = 3.2392 \times \left(\frac{I_{100}}{I_{110}}\right) + 0.4310 \quad (2)$$

The order parameter values for the quaternary, quinary, and senary alloys were approximated using Equation (2), and we found that the senary alloy possesses the highest chemical ordering with $L = 0.98$.

Table 1. Lattice parameter (a) and long-range order parameters (L) calculated from X-ray diffraction data.

| S. No. | Alloy | a | $(I_{100}/I_{110})_{Sample}$ | $(I_{100}/I_{110})_{Standard}$ | L |
|--------|----------------|--------|------------------------------|--------------------------------|--------|
| 1 | AlNi | 0.2870 | 0.147 | 0.176 | 0.92 |
| 2 | Al(CoFe) | 0.2880 | 0.166 | 0.180 | 0.96 |
| 3 | Al(FeNi) | 0.2890 | 0.096 | 0.176 | 0.74 |
| 4 | Al(CoNi) | 0.2871 | 0.121 | 0.181 | 0.82 |
| 5 | Al(CoFeNi) | 0.2867 | 0.145 | - | * 0.91 |
| 6 | Al(CoFeMnNi) | 0.2900 | 0.159 | - | * 0.95 |
| 7 | Al(CoCuFeMnNi) | 0.2917 | 0.169 | - | * 0.98 |

*—Calculated values from Equation (2).

Precision lattice parameter for the synthesized alloys was calculated using the Nelson–Riley method [43]. The calculated precision lattice parameter and intensity ratios are listed in the Table 1. It is seen that the order parameter is low in Fe-containing alloys and is high in alloys containing Co and Ni. Since the diffraction patterns represent the overall influence of all elements, it is not possible to comment on the site occupancies of individual elements in a multicomponent space from the X-ray diffraction data.

4.1.2. Microstructure and Composition Analysis

A detailed microstructure and compositional analysis of homogenised B2 aluminides was carried out using SEM-EDS. Figure 6 shows the SEM-BSE image of a binary AlNi and the corresponding elemental mapping after homogenization. The elemental distribution map obtained using SEM-EDS

shows a homogeneous distribution of Ni and Al. The overall composition of Al and Ni is presented in Table 2, and it was observed to be in the B2-phase field range.

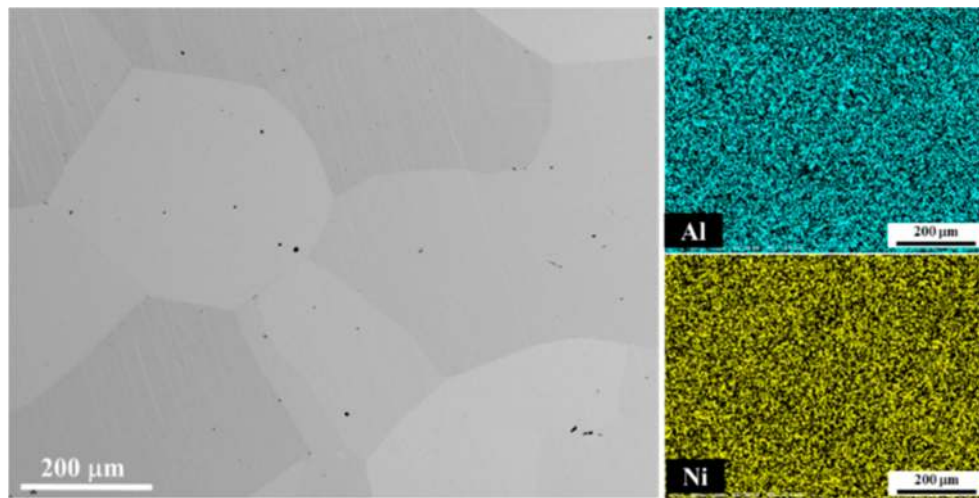


Figure 6. SEM-BSE image and elemental mapping of homogenized AlNi binary aluminide, homogenized at 1373 K for 144 h.

Table 2. Elemental compositions (at.%) in the homogenized multicomponent B2 aluminides.

| Alloy | Al | Co | Cu | Fe | Mn | Ni |
|----------------|----------|----------|---------|----------|----------|----------|
| AlNi | 51 ± 0.2 | - | - | - | - | 49 ± 0.2 |
| Al(CoNi) | 51 ± 0.2 | 24 ± 0.1 | - | - | - | 25 ± 0.2 |
| Al(FeNi) | 52 ± 0.1 | - | - | 24 ± 0.2 | - | 24 ± 0.2 |
| Al(CoFe) | 51 ± 0.2 | 25 ± 0.4 | - | 24 ± 0.6 | - | - |
| Al(CoFeNi) | 50 ± 0.6 | 16 ± 0.3 | - | 17 ± 0.3 | - | 17 ± 0.5 |
| Al(CoFeMnNi) | 50 ± 0.3 | 12 ± 0.1 | - | 12 ± 0.2 | 12 ± 0.2 | 12 ± 0.1 |
| Al(CoCuFeMnNi) | 50 ± 0.5 | 9 ± 0.3 | 9 ± 0.4 | 11 ± 0.5 | 10 ± 0.1 | 10 ± 0.1 |

The microstructures and corresponding elemental maps of the homogenized Al(CoNi), Al(FeNi), and Al(CoFe) ternary alloys are shown in Figure 7a–c. All alloys exhibit an equiaxed grain structure as seen in the BSE images of Figure 7a,c,e. The elemental maps in Figure 7 show that all the elements were homogeneously distributed throughout the microstructure upon homogenization annealing at 1373 K for 144 h. The SEM-BSE image and corresponding elemental mapping of quaternary Al(CoFeNi) are shown in Figure 8. A polycrystalline microstructure with equiaxed grains and uniform distribution of alloying elements was observed.

Figure 9a,b shows the microstructures and elemental maps for the quinary Al(CoFeMnNi) and senary Al(CoCuFeMnNi) alloys. A homogeneous, single-phase microstructure was observed in both the alloys, which is consistent with the CALPHAD predictions as well as XRD analysis. As discussed before, an equiatomic substitution of elements maximizing the overall configurational entropy of the Ni sublattice of the prototype B2-NiAl structure was designed. It is seen from the elemental mapping that all the alloying elements were uniformly distributed throughout the microstructure.

The elemental compositions of homogenized samples measured using SEM-EDS are summarized in Table 2. The average composition was determined from 10 independent measurements in different sample regions. It is seen that all the alloys contain compositions similar to their nominal values except for the slight enrichment of Al (about 1–2 at.%) in the binary and ternary alloys.

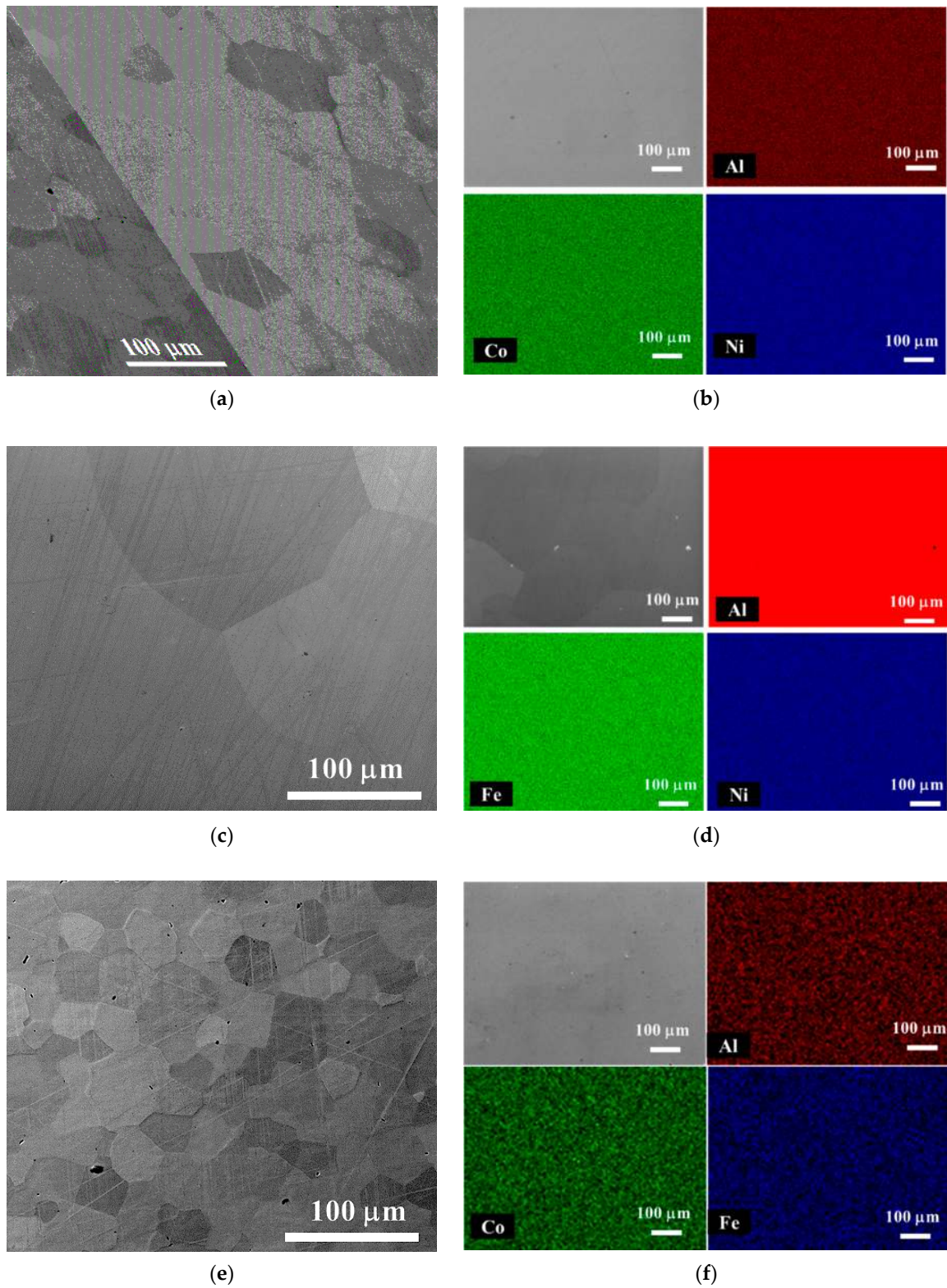


Figure 7. SEM-BSE image and corresponding elemental mapping of (a,b) Al(CoNi), (c,d) Al(FeNi), and (e,f) Al(CoFe) ternary alloys homogenized at 1373 K for 144 h.

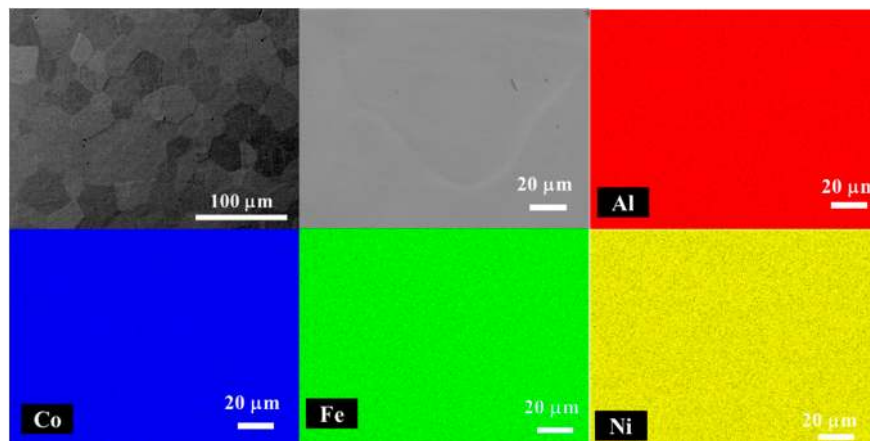
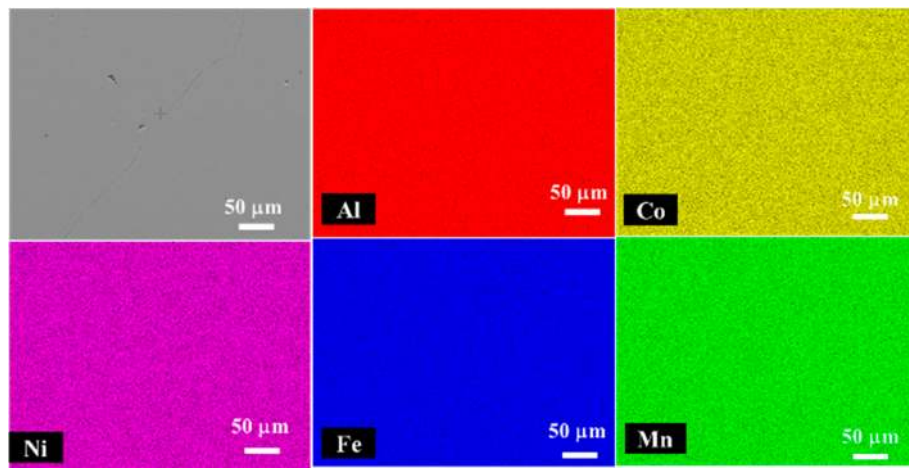
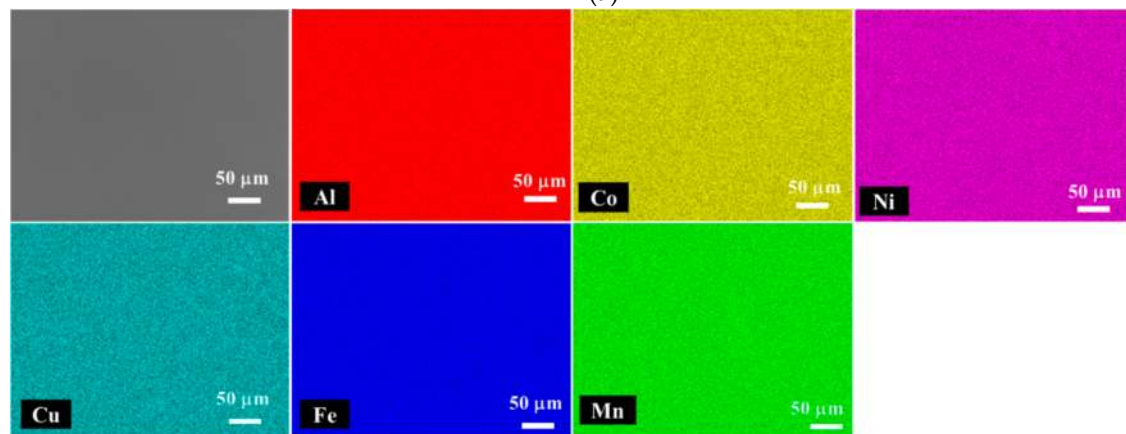


Figure 8. SEM-BSE image and elemental mapping of Al(CoFeNi) homogenized at 1373 K for 144 h.



(a)



(b)

Figure 9. SEM-BSE image and elemental mapping of the (a) Al(CoFeMnNi) and (b) Al(CoCuFeMnNi) multicomponent alloys homogenized at 1373 K for 144 h.

4.1.3. High Resolution STEM of Quinary and Senary B2 Aluminides

Overview HAADF-STEM images containing a grain boundary, corresponding STEM-EDS elemental maps, and atomically resolved HAADF-STEM images of the Al(CoFeMnNi) and Al(CoCuFeMnNi) alloys are shown in Figures 10 and 11, respectively. The contrast modulations in the overview HAADF-STEM images of Figures 10a and 11a stem from the FIB sample preparation. The elemental maps shown

in Figures 10a and 11a confirm a uniform distribution of the constituent elements within the bulk grains for both Al(CoFeMnNi) and Al(CoCuFeMnNi), respectively. In both cases, Mn segregation along the grain boundary is observed, whereas Cu is seen to uniformly distribute within the grain in the Al(CoCuFeMnNi) alloy shown in Figure 11a. The atomically resolved HAADF-STEM images of Figures 10b and 11b show the B-ordered lattice of Al(CoFeMnNi) and Al(CoCuFeMnNi) viewed along the (110) zone axis. The rows of atomic columns with bright contrast represent the Ni sublattice, and the rows with dark contrast represent the Al sublattice of the prototype B2 NiAl structure. The uniform contrast of both sublattices indicates a homogeneous distribution of alloying elements on the corresponding lattice sites. It should be noted that the atomic numbers (Z) of the Al sublattice is 13 and that of the corresponding elements on the TM sublattice is equal to ≈ 26.5 for Al(CoFeMnNi) and ≈ 26.9 for Al(CoCuFeMnNi), assuming a random distribution of elements according to the nominal composition. The possibility of anti-site defects and vacancies are excluded in these calculations.

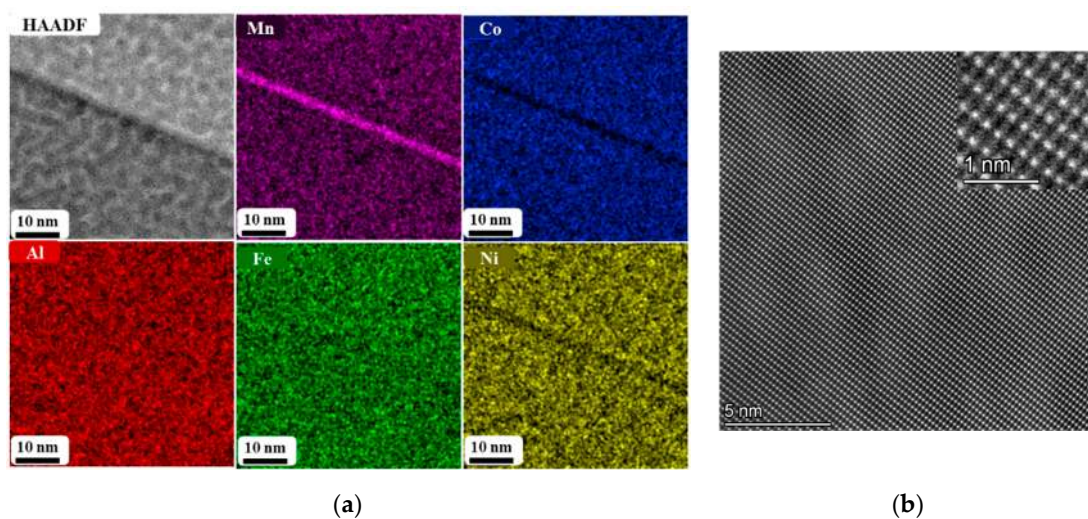


Figure 10. Aberration-corrected high angle annular dark-field (HAADF)-STEM analysis of Al(CoFeMnNi) B2 aluminide homogenized at 1373 K for 144 h shows (a) HAADF-STEM image and corresponding STEM-EDS elemental maps of constituent elements and (b) the atomically resolved HAADF-STEM image of the B2 ordered lattice.

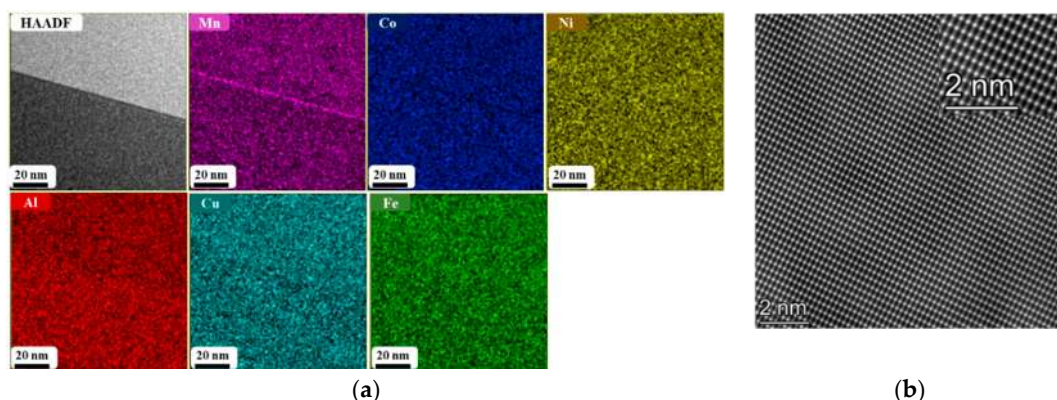


Figure 11. Aberration-corrected HAADF-STEM analysis of Al(CoCuFeMnNi) B2 aluminide shows (a) HAADF-STEM image and corresponding STEM-EDS elemental maps of constituent elements; (b) the atomically resolved HAADF-STEM image of the B2 ordered lattice.

Both vacancy (including so-called structural vacancies in Al-rich AlNi) and anti-site-types of defects are present in, for instance, stoichiometric AlNi or AlFe [44]. The concentration of Ni anti-sites, i.e., Ni atoms on the Al sublattice, approaches 10^{-4} at $0.7 T_m$ in Ni-rich AlNi alloys [44]. Such defects are

expected in the produced pseudo-binary HEAs as well. An experimental analysis of their concentrations is involved indeed and presents itself as a separate task (see e.g., the analysis of Pike et al. for the AlNiFe system [45]).

The chemical profiles across the grain boundary were analyzed by STEM-EDS mapping (Figure 12a,b). The Mn enrichment and depletion of Co and Ni along the grain boundaries is evident from the STEM-EDS line profile. Al is distributed uniformly along the grain boundary, and elements such as Co and Ni are depleted near the grain boundary but distributed uniformly inside the grains.

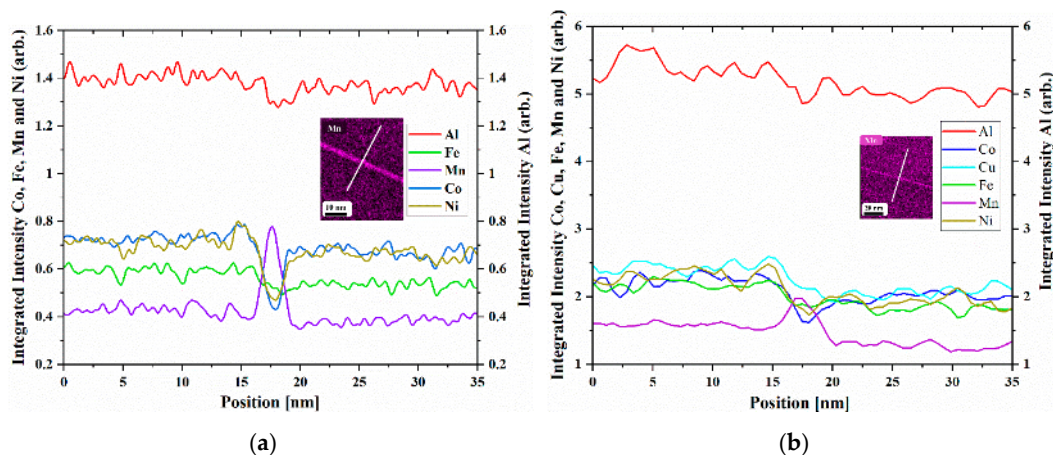


Figure 12. STEM-EDS composition line profile extracted across a grain boundary from the alloy (a) Al(CoFeMnNi) and (b) Al(CoCuFeMnNi) after humanizing for 144 h at 1373 K.

The aberration-corrected HAADF-STEM image of the Al(CoCuFeMnNi) alloy showing the atomic lattice of the B2 ordered phase and a hypothetical supercell of the multicomponent B2 crystal structure are given in Figure 13a,b, respectively. It is obvious from Figure 13a that the intensities of atomic columns representing the Al (dark columns) and Ni sublattice (bright columns) are uniform throughout the image, indicating a random distribution of TM on the Ni sublattice. However, since the intensity of an atomic column is an average of the contribution from different atomic species within the column, these intensities cannot be directly used to determine whether there is an additional degree of ordering within the Ni sublattice. As the Ni sublattice is substituted with multiple transition metal elements of similar atomic size and atomic number, it is assumed that the elements distribute randomly over the Ni sublattice. This proposed multicomponent supercell with the B2 structure is shown in Figure 13b. As can be seen from Figure 13b, the Al atoms occupy the body-centered positions, and Co, Cu, Fe, Mn, and Ni are randomly distributed on the Ni sites of the B2-NiAl prototype structure.

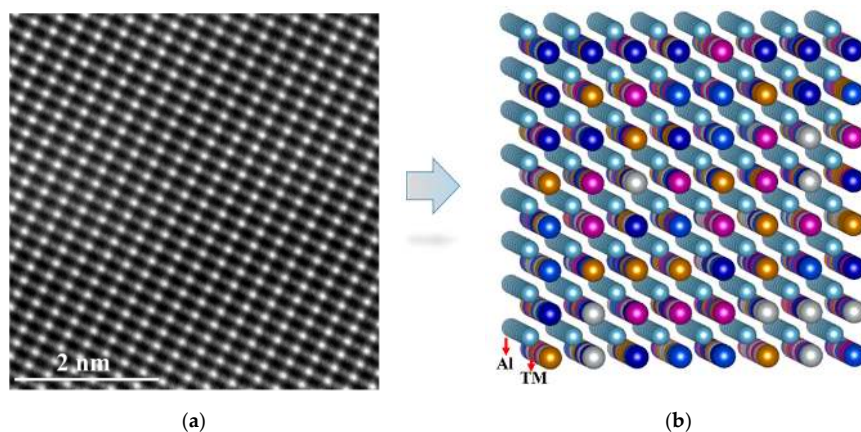


Figure 13. (a) Fourier-filtered atomic resolution HAADF-STEM image of the Al(CoCuFeMnNi) alloy. (b) Proposed unit cell showing the Al and (CoCuFeMnNi) transition metal sublattice.

4.2. Thermal Analysis (DTA) and Heat Treatment

A differential thermal analysis of the multicomponent aluminides was performed to understand the phase stability of obtained B2 phase and to measure the melting point of the alloys. As shown in Figure 14a–f, endothermic peaks corresponding to the melting temperature are observed. As the melting point of Al(CoNi) is above the feasible temperature range in the DTA, the calculated melting point from CALPHAD was used. For the majority of the investigated alloys, the calculated melting points are in a good agreement with the measured values given in Table 3. Only in the case of Al(CoCuFeMnNi) the predicted and measured melting temperatures deviate largely in comparison to other alloys.

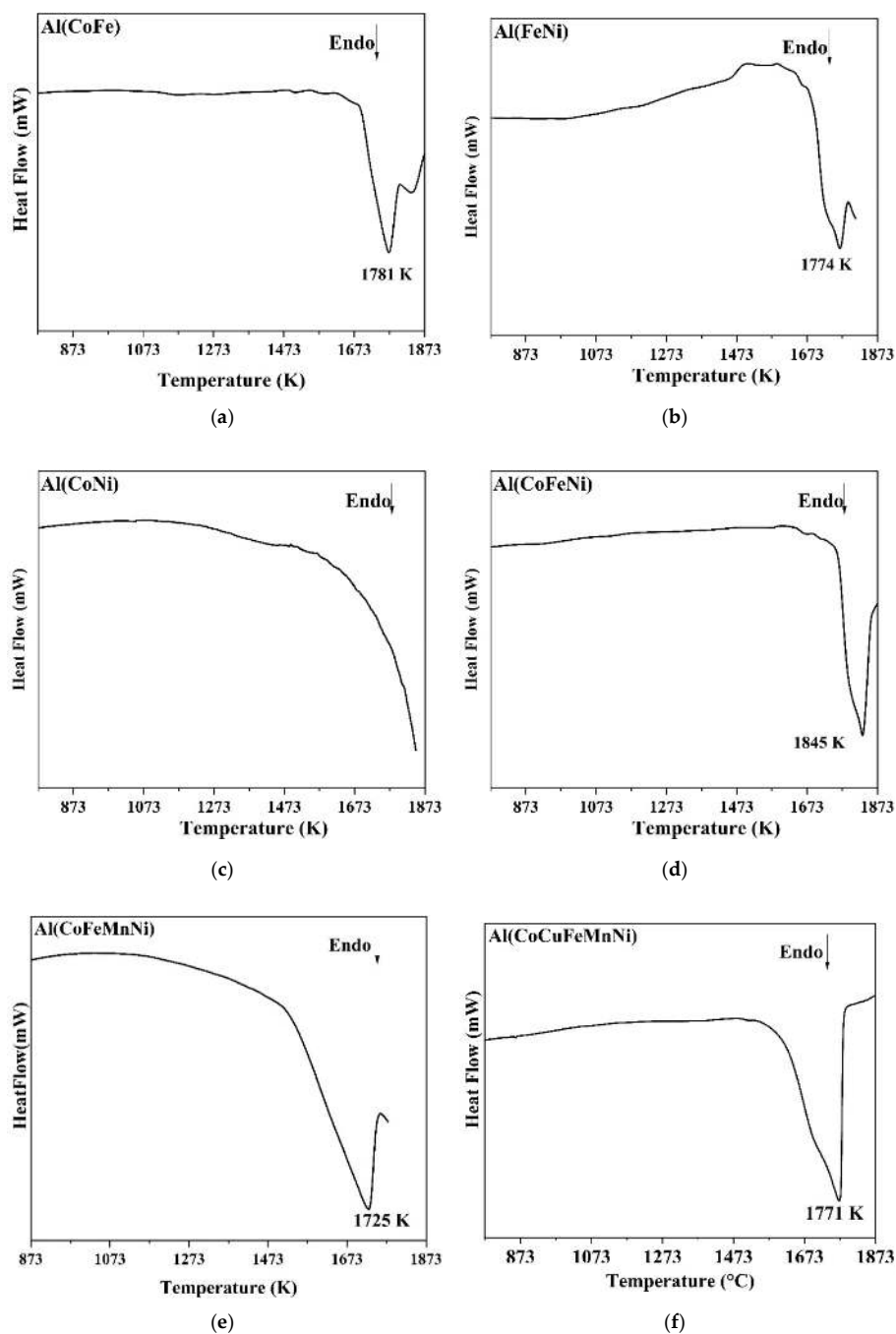


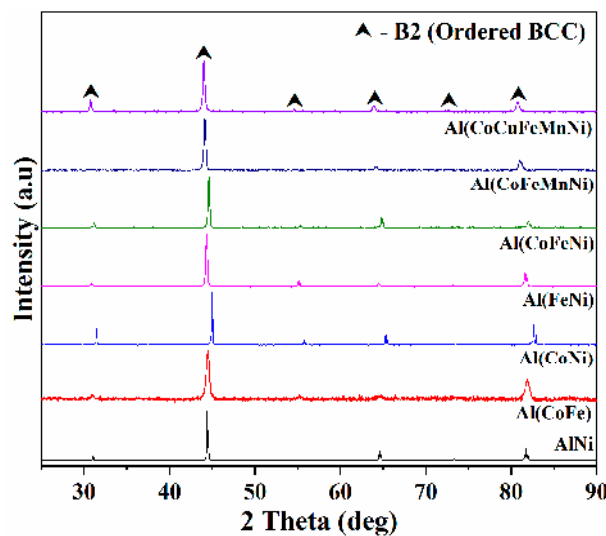
Figure 14. Heat flow curves obtained from the differential thermal analysis (DTA) of (a) Al(CoFe), (b) Al(FeNi), (c) Al(CoNi), (d) Al(CoFeNi), (e) Al(CoFeMnNi), and (f) Al(CoCuFeMnNi).

Table 3. Comparison of calculated and measured (DTA) melting points of pseudo-binary aluminides.

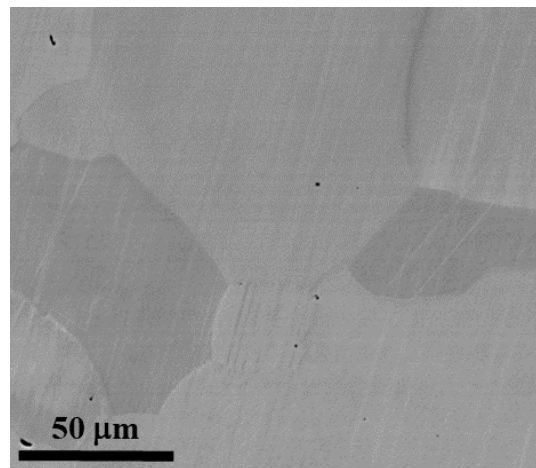
| S.No. | Alloy | T_{melting} (K) | |
|-------|----------------|--------------------------|----------|
| | | Calculated | Measured |
| 1 | AlNi | 1954 | 1911 |
| 2 | Al(CoFe) | 1725 | 1781 |
| 3 | Al(FeNi) | 1763 | 1774 |
| 4 | Al(CoNi) | 1984 | - |
| 5 | Al(CoFeNi) | 1864 | 1845 |
| 6 | Al(CoFeMnNi) | 1730 | 1725 |
| 7 | Al(CoCuFeMnNi) | 1676 | 1771 |

A decomposition or precipitation of secondary phases in HEAs is known to be observed after long-term heat treatments [14]. Hence, it is essential to understand the thermal stability of the produced alloys under isothermal heat treatments for prolonged annealing times. Studies on thermal stability of these alloys are performed at two temperatures, i.e., intermediate (1073 K) and enhanced (1373 K) ones. As mentioned before, the synthesized alloys were homogenized at 1373 K for 144 h. The aforementioned results of the alloys after prolonged annealing confirm the excellent stability of B2 phase at 1373 K.

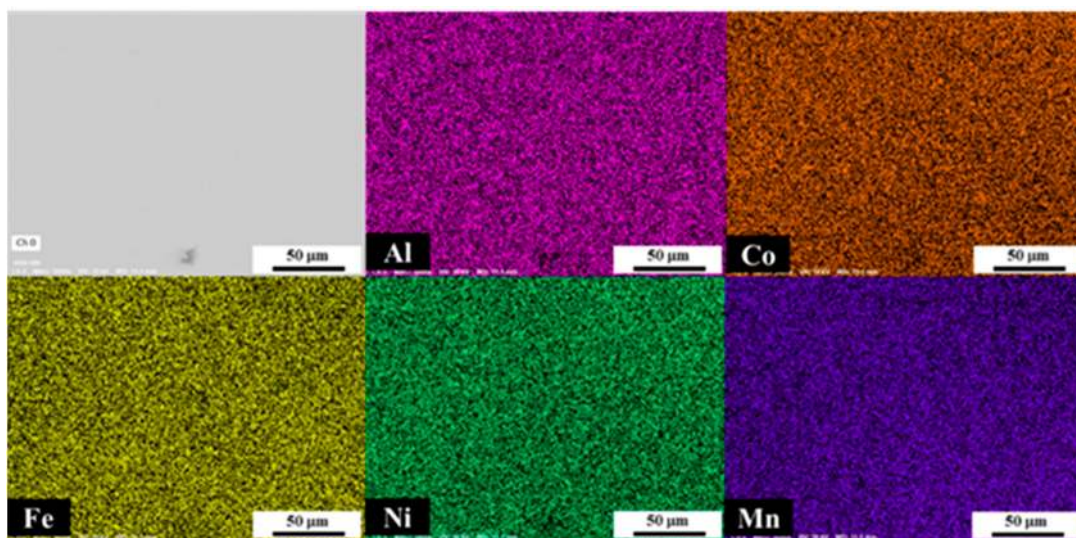
Figure 15 shows the XRD patterns of multicomponent B2 aluminides heat treated at 1073 K for 200 h. The B2 phase was observed to be stable after prolonged heat treatment. It is seen in the XRD patterns that the superlattice reflections corresponding to (100), (111), and (210) crystallographic planes appeared along with the fundamental reflections (110), (200), and (211). The peaks corresponding to any other phases were not observed. The XRD patterns were observed to be similar to the patterns of homogenized samples (Figure 5a,b).

**Figure 15.** X-ray diffractograms of pseudo-binary multicomponent alloys annealed at 1073 K for 200 h showing the ordered BCC (B2) structure.

An example of the microstructure and elemental distribution after the prolonged heat treatments are shown in Figure 16, which substantiates a homogeneous distribution of constituent elements after annealing at 1073 K for 200 h. All other alloys were observed to have similar homogenous distribution of elements after heat treatments. A single-phase microstructure seen in Figure 16a confirms the excellent thermal stability of the synthesized multicomponent aluminides with the B2 structure.



(a)



(b)

Figure 16. (a) SEM-BSE image. (b) Corresponding elemental mapping of Al(CoFeMnNi) quinary alloy heat treated at 1073 K, for 200 h.

5. Conclusions

- Multicomponent B2-ordered aluminide compositions, namely, Al(CoNi), Al(CoFe), Al(FeNi), Al(CoFeNi), Al(CoFeMnNi), and Al(CoCuFeMnNi), were designed through a heuristic phase diagram inspection, a pseudo-binary approach, and a CALPHAD analysis.
- Multicomponent single-phase B2-ordered aluminides were synthesized successfully through arc melting followed by suction casting.
- Multiple characterization techniques were utilized to investigate the microstructure of the alloys. All the B2 aluminides were observed to be single phase, and a homogeneous distribution of elements was verified by SEM-EDS elemental maps.
- The XRD results indicate the presence of superlattice reflections, substantiating the presence of the B2 phase in all the alloys. The order parameter, L , was calculated until the ternary alloys and found to be highest for Al(CoFe) ($L = 0.96$) and is lowest for Al(FeNi) ($L = 0.74$).
- The order parameter for the alloys with a higher number of elements (quinary to senary) was not determined, as the standard database was not available. However, the ratio of the superlattice to

fundamental reflections (I_{100}/I_{110}) was used to approximate the order parameter in higher-order systems (quaternary, quinary, and senary alloys), and the maximum order parameter in senary alloy was found to be 0.98.

- TEM results confirmed the presence of B2 ordering in the alloys. The STEM-EDS elemental maps show a slight segregation of Mn along grain boundaries. All the elements were observed to be uniformly distributed inside the grains.
- The thermal stability of multicomponent B2 aluminides was investigated at 1373 and 1073 K. The B2 phase was observed to be stable even after prolonged annealing up to 200 h.
- The phase evolution and the stability in the present B2 aluminides were in accordance with the assumptions made using the matching element method as well as CALPHAD predictions.
- The experimental results indicate that the strategies followed for composition design were very effective in designing multicomponent single-phase B2 alloys.

Author Contributions: Conceptualization, B.S.M. and G.M.M.; methodology, G.M.M.; software, K.G.; validation, K.G. and G.M.M.; formal analysis, G.M.M., A.C.M.E., B.S.M., K.N.K., C.H.L., S.V.D., and G.W.; investigation, G.M.M. and P.W.; resources, B.S.M., C.H.L., S.V.D., and G.W.; data curation, G.M.M., A.C.M.E.; writing—original draft preparation, G.M.M.; writing—review and editing, G.M.M., A.C.M.E., K.G., B.S.M., K.N.K., S.V.D., C.H.L., P.W., and G.W.; visualization, G.M.M., A.C.M.E.; supervision, B.S.M., K.N.K., S.V.D., and G.W.; funding acquisition, B.S.M., S.V.D., G.W., and C.H.L. All authors have read and agreed to the published version of the manuscript.

Funding: This research was partially funded by the German Science Foundation (DFG), grant numbers DI 1419/11-1 and LI 2133/4-1.

Acknowledgments: G.M.M. is grateful to the German academic exchange service (DAAD) for awarding a fellowship to conduct experiments at the University of Münster, Germany. A.C.M.E. would like to thank the Alexander von Humboldt (AvH) foundation in Germany for awarding a fellowship. A partial financial support from the German Science Foundation (DFG), project number DI 1419/11-1 and LI 2133/4-1, was acknowledged.

Conflicts of Interest: The authors declare no conflict of interest.

References

1. Diao, H.Y.; Feng, R.; Dahmen, K.A.; Liaw, P.K. Fundamental deformation behavior in high-entropy alloys: An overview. *Curr. Opin. Solid State Mater. Sci.* **2017**, *21*, 252–266. [[CrossRef](#)]
2. Li, Z.; Raabe, D. Strong and Ductile Non-equiatomic High-Entropy Alloys: Design, Processing, Microstructure, and Mechanical Properties. *JOM* **2017**, *69*, 2099–2106. [[CrossRef](#)] [[PubMed](#)]
3. Sriharitha, R.; Murty, B.S.; Kottada, R.S. Alloying, thermal stability and strengthening in spark plasma sintered $\text{Al}_x\text{CoCrCuFeNi}$ high entropy alloys. *J. Alloy. Compd.* **2014**, *583*, 419–426. [[CrossRef](#)]
4. Zhao, J.H.; Ji, X.L.; Shan, Y.P.; Fu, Y.; Yao, Z. On the microstructure and erosion-corrosion resistance of AlCrFeCoNiCu high-entropy alloy via annealing treatment. *Mater. Sci. Technol. U.K.* **2016**, *32*, 1271–1275. [[CrossRef](#)]
5. Yu, Y.; Wang, J.; Li, J.S.; Kou, H.C.; Niu, S.Z.; Zhu, S.Y.; Yang, J.; Liu, W.M. Dry-sliding tribological properties of AlCoCrFeNiTi0.5 high-entropy alloy. *Rare Met.* **2017**, *1*–7. [[CrossRef](#)]
6. Butler, T.M.; Weaver, M.L. Oxidation behavior of arc melted AlCoCrFeNi multi-component high-entropy alloys. *J. Alloy. Compd.* **2016**, *674*, 229–244. [[CrossRef](#)]
7. Chokshi, A.H. High temperature deformation in fine grained high entropy alloys. *Mater. Chem. Phys.* **2017**. [[CrossRef](#)]
8. Yeh, J.W. Recent progress in high-entropy alloys. *Ann. Chim. Sci. Des Mater.* **2006**, *31*, 633–648. [[CrossRef](#)]
9. Yeh, J.-W.; Lin, S.-J.; Chin, T.-S.; Gan, J.-Y.; Chen, S.-K.; Shun, T.-T.; Tsau, C.-H.; Chou, S.-Y. Formation of simple crystal structures in $\text{Cu-Co-Ni-Cr-Al-Fe-Ti-V}$ alloys with multiprincipal metallic elements. *Met. Mater. Trans. A* **2004**, *35*, 2533–2536. [[CrossRef](#)]
10. Murty, B.S.; Ranganathan, S.; Yeh, J.W.; Bhattacharjee, P.P. *High-Entropy Alloys*; Elsevier: Amsterdam, The Netherlands, 2019; ISBN 9780128160671.
11. Yeh, J.W.; Liaw, P.K.; Gao, M.C.; Zhang, Y. (Eds.) *High-Entropy Alloys: Fundamentals and Applications*; Springer International Publishing: Cham, Germany, 2016; ISBN 978-3-319-27013-5.
12. Cantor, B.; Chang, I.T.H.; Knight, P.; Vincent, A.J.B. Microstructural development in equiatomic multicomponent alloys. *Mater. Sci. Eng. A* **2004**, *375–377*, 213–218. [[CrossRef](#)]

13. Otto, F.; Dlouhý, A.; Pradeep, K.G.; Kuběnová, M.; Raabe, D.; Eggeler, G.; George, E.P. Decomposition of the single-phase high-entropy alloy CrMnFeCoNi after prolonged anneals at intermediate temperatures. *Acta Mater.* **2016**, *112*, 40–52. [[CrossRef](#)]
14. Laplanche, G.; Berglund, S.; Reinhart, C.; Kostka, A.; Fox, F.; George, E.P. Phase stability and kinetics of σ -phase precipitation in CrMnFeCoNi high-entropy alloys. *Acta Mater.* **2018**, *161*, 338–351. [[CrossRef](#)]
15. Glienke, M.; Vaidya, M.; Gururaj, K.; Daum, L.; Tas, B.; Rogal, L.; Pradeep, K.G.; Divinski, S.V.; Wilde, G. Grain boundary diffusion in CoCrFeMnNi high entropy alloy: Kinetic hints towards a phase decomposition. *Acta Mater.* **2020**, *195*, 304–316. [[CrossRef](#)]
16. Li, C.; Zhao, M.; Li, J.C.; Jiang, Q. B2 structure of high-entropy alloys with addition of Al. *J. Appl. Phys.* **2008**, *104*. [[CrossRef](#)]
17. Vaidya, M.; Muralikrishna, G.M.; Murty, B.S. High-entropy alloys by mechanical alloying: A review. *J. Mater. Res.* **2019**, *34*, 664–686. [[CrossRef](#)]
18. Garlapati, M.M.; Vaidya, M.; Karati, A.; Mishra, S.; Bhattacharya, R.; Murty, B.S. Influence of Al content on thermal stability of nanocrystalline Al_xCoCrFeNi high entropy alloys at low and intermediate temperatures. *Adv. Powder Technol.* **2020**, *31*, 1985–1993. [[CrossRef](#)]
19. Wang, Y.; Yang, Y.; Yang, H.; Zhang, M.; Ma, S.; Qiao, J. Microstructure and wear properties of nitrated AlCoCrFeNi high-entropy alloy. *Mater. Chem. Phys.* **2017**, *210*, 233–239. [[CrossRef](#)]
20. Moravcik, I.; Cizek, J.; Gavendova, P.; Sheikh, S.; Guo, S.; Dlouhy, I. Effect of heat treatment on microstructure and mechanical properties of spark plasma sintered AlCoCrFeNiTi_{0.5} high entropy alloy. *Mater. Lett.* **2016**, *174*, 53–56. [[CrossRef](#)]
21. Nagase, T.; Takemura, M.; Matsumuro, M.; Maruyama, T. Solidification Microstructure of AlCoCrFeNi_{2.1} Eutectic High Entropy Alloy Ingots. *Mater. Trans.* **2018**, *59*, 255–264. [[CrossRef](#)]
22. Reddy, T.S.; Wani, I.S.; Bhattacharjee, T.; Reddy, S.R.; Saha, R.; Bhattacharjee, P.P. Severe plastic deformation driven nanostructure and phase evolution in a Al_{0.5}CoCrFeMnNi dual phase high entropy alloy. *Intermetallics* **2017**, *91*, 150–157. [[CrossRef](#)]
23. Tsai, C.W.; Tsai, M.H.; Yeh, J.W.; Yang, C.C. Effect of temperature on mechanical properties of Al_{0.5}CoCrCuFeNi wrought alloy. *J. Alloy. Compd.* **2010**, *490*, 160–165. [[CrossRef](#)]
24. Butler, T.M.; Alfano, J.P.; Martens, R.L.; Weaver, M.L. High-Temperature Oxidation Behavior of Al-Co-Cr-Ni-(Fe or Si) Multicomponent High-Entropy Alloys. *JOM* **2015**, *67*, 246–259. [[CrossRef](#)]
25. Westbrook, J.H.; Fleischer, R.L. *Basic Mechanical Properties and Lattice Defects of Intermetallic Compounds*; John Wiley & Sons Ltd: New York, NY, USA, 2000; ISBN 0471611751.
26. Miracle, D.B. The physical and mechanical properties of NiAl. *Acta Met. Mater.* **1993**, *41*, 649–684. [[CrossRef](#)]
27. Baker, I. A review of the mechanical properties of B2 compounds. *Mater. Sci. Eng. A* **1995**, *192–193*, 1–13. [[CrossRef](#)]
28. Girifalco, L.A. Vacancy concentration and diffusion in order-disorder alloys. *J. Phys. Chem. Solids* **1964**, *24*, 323–333. [[CrossRef](#)]
29. Mohan Muralikrishna, G.; Vaidya, M.; Murty, B.S.; Divinski, S.V.; Wilde, G. Tracer diffusion in ordered pseudo-binary multicomponent aluminides. *Scr. Mater.* **2020**, *178*, 227–231. [[CrossRef](#)]
30. Muralikrishna, G.M.; Esin, V.A.; Kulkarni, K.N.; Murty, B.S.; Wilde, G.; Divinski, S.V. Atomic transport in B2-ordered Al(Fe,Ni) alloys: Tracer-interdiffusion couple approach. *Intermetallics* **2020**, *126*. [[CrossRef](#)]
31. Kim, K.B.; Warren, P.J.; Cantor, B. Formation of Metallic Glasses in Novel (Ti₃₃Zr₃₃Hf₃₃)_{100-x-y}(Ni₅₀Cu₅₀)_xAl_y Alloys. *Mater. Trans.* **2003**, *44*, 411–413. [[CrossRef](#)]
32. Guo, S.; Ng, C.; Lu, J.; Liu, C.T. Effect of valence electron concentration on stability of fcc or bcc phase in high entropy alloys. *J. Appl. Phys.* **2011**, *109*. [[CrossRef](#)]
33. Zhang, F.; Zhang, C.; Chen, S.L.; Zhu, J.; Cao, W.S.; Kattner, U.R. An understanding of high entropy alloys from phase diagram calculations. *Calphad Comput. Coupling Phase Diagr.* **2014**, *45*, 1–10. [[CrossRef](#)]
34. Massalski, T.B.; Okamoto, H. *Binary Alloy Phase Diagrams*, 2nd ed.; ASM International: Russel Township, OH, USA, 1990.
35. Alloy Phase Diagrams. *ASM Handbook*; ASM International: Russel Township, OH, USA, 1992; Volume 3.
36. Saunders, N.; Miodownik, A.P. (Eds.) *CALPHAD Calculation of Phase Diagrams: A Comprehensive Guide*; Pergamon Materials Series; Pergamon: Oxford, UK, 1998; Volume 1, ISBN 0080421296.
37. Mao, H.; Chen, H.C.Q. TCHEA1: A Thermodynamic Database Not Limited for “High Entropy” Alloys. *J. Phase Equilibria Diffus.* **2017**, *38*. [[CrossRef](#)]

38. Chen, H.; Mao, H.; Chen, Q. Database development and Calphad calculations for high entropy alloys: Challenges, strategies, and tips. *Mater. Chem. Phys.* **2018**, *210*, 279–290. [[CrossRef](#)]
39. Rogal, L.; Bobrowski, P.; Körmann, F.; Divinski, S.; Stein, F.; Grabowski, B. Computationally-driven engineering of sublattice ordering in a hexagonal AlHfScTiZr high entropy alloy. *Sci. Rep.* **2017**, *7*, 1–14. [[CrossRef](#)]
40. Ikeda, Y.; Grabowski, B.; Körmann, F. Ab initio phase stabilities and mechanical properties of multicomponent alloys: A comprehensive review for high entropy alloys and compositionally complex alloys. *Mater. Charact.* **2019**, *147*, 464–511. [[CrossRef](#)]
41. Li, Z.; Körmann, F.; Grabowski, B.; Neugebauer, J.; Raabe, D. Ab initio assisted design of quinary dual-phase high-entropy alloys with transformation-induced plasticity. *Acta Mater.* **2017**, *136*, 262–270. [[CrossRef](#)]
42. Cullity, B.D.; Stock, S.R. *Elements of X-ray Diffraction*; Pearson Education: London, UK, 1978; ISBN 0201610914.
43. Tsai, D.S.; Chin, T.S.; Hsu, S.E.; Hung, M.P. A Simple Method for the Determination of Lattice Parameters from Powder X-ray Diffraction Data. *Mater. Trans. JIM* **1989**, *30*, 474–479. [[CrossRef](#)]
44. Paul, A.; Divinski, S.V. *Handbook of Solid State Diffusion: Diffusion Fundamentals and Techniques*; Elsevier: Amsterdam, The Netherlands, 2017; Volume 1, pp. 449–517. ISBN 9780128042878.
45. Pike, L.M.; Anderson, I.M.; Liu, C.T.; Chang, Y.A. Site occupancies, point defect concentrations, and solid solution hardening in B2 (Ni,Fe)Al. *Acta Mater.* **2002**, *50*, 3859–3879. [[CrossRef](#)]

Publisher’s Note: MDPI stays neutral with regard to jurisdictional claims in published maps and institutional affiliations.



© 2020 by the authors. Licensee MDPI, Basel, Switzerland. This article is an open access article distributed under the terms and conditions of the Creative Commons Attribution (CC BY) license (<http://creativecommons.org/licenses/by/4.0/>).